

# Nonlinear magnetohydrodynamics of pulsed parallel current drive in reversed-field pinches

J. M. Reynolds,<sup>a)</sup> C. R. Sovinec, and S. C. Prager  
*University of Wisconsin-Madison, Madison, Wisconsin 53706, USA*

(Received 28 April 2008; accepted 9 May 2008; published online 27 June 2008)

Nonlinear simulation with a simple resistive magnetohydrodynamics model is used to investigate the stabilization of magnetic fluctuations in reversed-field pinch plasmas subject to pulsed-parallel current drive. Numerical results are diagnosed with computations of nonlinear power transfer and by evaluating sequences of profiles for linear stability. Results show that poloidal electric field pulsing promptly affects the exchange of energy between the mean profiles and both core-resonant  $m=1$  fluctuations and high-axial-wavenumber fluctuations. Linear computations show that slight changes in edge profiles are sufficient to alter the stability of the marginal state. There is a slight delay in the response of energy exchanged among fluctuations, which reduces the  $m=0$  fluctuations. Loss of dynamo effect as fluctuation amplitudes decrease leads to nonlocal pulse penetration that enhances pinching when toroidal drive is maintained. Reducing toroidal drive together with the application of poloidal electric field avoids pinching and maintains the stabilizing effect for a greater period of time. © 2008 American Institute of Physics. [DOI: 10.1063/1.2937770]

## I. INTRODUCTION

The magnetic field in reversed-field pinch (RFP) configurations is strongly sheared from the magnetic axis outward and is largely poloidal over most of the plasma volume. Toroidal electric field from standard Ohmic induction therefore drives current in the plasma core while bypassing the edge region. Current-gradient-driven instabilities result from this spatially preferential drive, and saturated fluctuations sustain reversed toroidal field in the plasma edge<sup>1</sup> through a magnetohydrodynamic (MHD) dynamo effect. The nonlinear interaction of resonant fluctuations with different helicity leads to regions of stochastic magnetic topology, allowing parallel heat flow to carry thermal energy from the core to the edge. The transport of energy results from the correlation of parallel heat flow fluctuations and radial magnetic perturbations, and this process, i.e. the correlated product, has been measured<sup>2</sup> in the Madison Symmetric Torus (MST).<sup>3</sup> While standard Ohmic drive produces configurations with a peak temperature of hundreds of eV, the energy confinement is low relative to the ideal situation of nested magnetic flux surfaces.

The existence of tearing-mode stable RFP equilibria<sup>4,5</sup> allows a direct path to better confinement through current-profile control if suitable current-drive techniques can be applied. Many successful demonstrations of fluctuation suppression have been achieved in MST through transient pulsing of the inductive electric field,<sup>6–8</sup> leading to order of magnitude increases in energy confinement time.<sup>9–12</sup> The earliest experiments used pulses of poloidal electric field alone. However, the best performance is achieved when the toroidal electric field is simultaneously reduced<sup>12</sup> so that the change in applied electric field remains parallel to the edge magnetic field. The experiments have therefore been labeled “pulsed

parallel current drive” (PPCD). Profile evolution, reconstructed through MHD equilibrium calculations, has shown that dynamo-free conditions are achieved in some experiments.<sup>7,8</sup> The nonzero component of the applied poloidal electric field reduces the toroidal magnetic flux in the system, so the conditions are transient. In fact, reducing both toroidal electric field and toroidal flux is in common with the proposed self-similar decay approach<sup>13</sup> to creating tearing-stable RFP plasmas and with part of the oscillating field current-drive cycle.<sup>14</sup>

The nonlinear aspects of combining standard inductive drive with current profile control in RFPs are considered computationally in Ref. 15 for sustained DC helicity injection in the resistive MHD model without pressure. A study with a localized ad hoc source of parallel current finds that auxiliary drive located midway between the core and edge of RFP profiles excites edge-resonant modes while stabilizing core-resonant modes. However, complete suppression of fluctuations is obtained through auxiliary drive located just inside the reversal surface in combination with reduced Ohmic drive.<sup>16</sup>

Nonlinear modeling specific to PPCD has shown that the evolution of the profile includes a significant pinching effect when the toroidal drive is not reduced.<sup>17</sup> The stabilization of fluctuations and subsequent loss of dynamo leads to nonlocal penetration of electric field after the pulse is applied in these three-dimensional computations. A study with a reduced set of modes but finite pressure emphasizes the potential role of magnetic shear when the pressure gradient adds to the available free energy.<sup>18</sup> Another study uses a quasilinear-like approach of applying pulsing to a one-dimensional evolution of the equilibrium while monitoring linear stability. The computations use realistic values of Lundquist number ( $S = \tau_r / \tau_A$ , where  $\tau_r$  is the resistive diffusion time and  $\tau_A$  is the Alfvén propagation time) and allow a vacuum gap to open between the plasma and the wall when the pulse is applied.

<sup>a)</sup>Present address: Los Alamos National Laboratory, Los Alamos, NM 87545, USA.

The resistivity profile is nearly uniform through the plasma region, but increases near the wall. The modification in edge current by the applied poloidal electric field is found to alter the equilibrium to a sufficient degree to make resonant tearing modes stable.<sup>19</sup> In Ref. 17, it is noted that an edge current is absent in three-dimensional simulations that show nonlocal pulse penetration due to dynamo loss.

The goal of the present work is to analyze MHD stabilization through PPCD consistent with profile evolution that occurs directly from the pulse and indirectly through dynamo loss. We apply three-dimensional numerical computations to the pressureless resistive MHD model subject to boundary conditions that represent the poloidal pulse either alone or together with a decrease in the toroidal electric field. Moreover, we use computational diagnostics of power-transfer between the evolving large-scale fields and the fluctuations, and among groups of fluctuations, to investigate how fluctuation suppression occurs while nonlinear effects are significant. Similar diagnostics have proven to be very useful in describing the MHD dynamo effect in standard RFP conditions.<sup>20</sup> To augment the nonlinear power analysis, we also investigate the linear stability of the evolving profiles. While linear analysis cannot provide a full description of the nonlinear system, it helps us distinguish the part of the profile evolution that is responsible for the change in power transfer from the mean fields to the fluctuations. Here, we will show that a very slight increase in edge current density immediately after application of the pulse is sufficient to alter the flow of power through the saturated fluctuations. While this is similar to the conclusions of Ref. 19, we show that it is also consistent with pinching due to loss of dynamo, which can dominate the subsequent profile evolution, as discussed in Ref. 17. The reduction in loop voltage, which is necessary to optimize performance in MST, is found to counter this pinching, maintaining a stable profile throughout the pulse.

The second section of this paper describes the MHD system used in our study, the boundary conditions used to apply PPCD transients, and the computational diagnostics. As a benchmark case, the third section considers the classical evolution of cylindrically symmetric profiles subject to pulsing without the inclusion of instabilities. The fourth section considers PPCD and evolution with a system that is limited to have only one resonant fluctuation. This simplifies the dynamics by eliminating coupling among groups of fluctuations and helps illustrate how suppression of dynamo activity leads to nonlocal pulse penetration. The fifth section describes analysis of PPCD in a full RFP simulation with nonlinear interaction. Conclusions from this study are provided in the sixth section.

## II. PPCD MODELING

The primary models of PPCD used in this study solve the time-dependent nonlinear resistive MHD equations in the limit of vanishing plasma pressure. Similar modeling has proven valuable for the RFP configuration in describing the MHD dynamo resulting from current-driven modes,<sup>21</sup> nonlinear cascading processes,<sup>22,23</sup> nonlinear power transfer,<sup>20</sup>

and increasing intermittency as  $S$  is increased.<sup>24</sup> The spectrum in these simulations is dominated by multiple  $m=1$  fluctuations that are resonant in the core, where  $m$  refers to the azimuthal or poloidal Fourier index, and  $n$  refers to the axial or toroidal index in helical  $e^{i(m\theta-2\pi n z/L_z)}$  components. In addition, while computational practicalities limit dimensionless parameters relative to laboratory conditions, applying the  $S$ -scaling found from computation<sup>24</sup> to the 3% simulated fluctuation level agrees reasonably well with the 1% level found in experiment.<sup>25</sup> This simplified resistive MHD system in MKS units is

$$\rho \left( \frac{\partial}{\partial t} \mathbf{V} + \mathbf{V} \cdot \nabla \mathbf{V} \right) = \mathbf{J} \times \mathbf{B} + \nabla \cdot \rho \nu \nabla \mathbf{V}, \quad (1)$$

$$\frac{\partial}{\partial t} \mathbf{B} = \nabla \times \left( \mathbf{V} \times \mathbf{B} - \frac{\eta}{\mu_0} \nabla \times \mathbf{B} \right), \quad (2)$$

where  $\mathbf{V}$  is the plasma flow velocity,  $\mathbf{B}$  is the magnetic field,  $\nu$  is the viscous diffusivity for a basic kinematic stress, and  $\eta/\mu_0$  is the magnetic diffusivity.

In this model, the mass density  $\rho$  is considered to be constant; however, compressibility is not constrained. This leads to known errors in momentum conservation and energy conservation, where the loss rates per unit volume are  $\rho \mathbf{V} \nabla \cdot \mathbf{V}$  and  $\rho V^2 \nabla \cdot \mathbf{V}/2$ , respectively. The scaling argument provided in the Appendix indicates that both errors are small when  $S$  is large, and this has been confirmed in simulation results. While it is possible to solve more comprehensive models of PPCD than Eqs. (1) and (2), this system minimizes the number of nonlinearities and permits investigating a larger number of transient events for a given amount of computational resources. Simulations of PPCD that include continuity and anisotropic thermal conduction<sup>26</sup> have shown similar stabilization effects.

The simplified model is solved in cylindrical geometry using the NIMROD code.<sup>27</sup> Without pressure-driven modes, toroidal curvature does not have a strong influence on the MHD activity, and a comparison of RFP simulations in cylindrical and toroidal geometry finds similar spectra in standard multihelicity conditions.<sup>28</sup> The study reported here uses the finite Fourier representation for the axial direction of the cylinder and high-order finite elements for the radial-azimuthal plane. Thus, our simulated fluctuations are easily decomposed by toroidal index  $n$ . Most of our computations use  $S=8000$  and  $Pm=1$ , where  $Pm=\mu_0\nu/\eta$ . The nominal values of magnetic and viscous diffusivity are multiplied by the function  $[1+(\sqrt{10}-1)(r/a)^{10}]^2$  to create a hollow profile in radius. A numerical convergence study of the nonlinear fluctuation level in RFP simulations in these conditions uses a  $24 \times 32$  mesh of elements, increasing the degree of the polynomial basis functions from bicubic to biquintic to improve resolution. There is increasingly detailed agreement in the fluctuation level history with a discrepancy of less than 3% over the PPCD timescale used in our study.<sup>29</sup> The results reported here use biquartic elements. The number of axial Fourier components is intentionally varied among different

sets of simulations to control the importance of nonlinear interaction. The full RFP simulations described in Sec. V include  $0 \leq n \leq 42$ .

The weak form of the equations solved by the code is readily adapted to applying the PPCD transients. The weak form of Faraday's law includes the surface term  $\oint d\mathbf{S} \times \mathbf{E} \cdot \mathbf{c}$ , where  $\mathbf{c}$  is a vector test function and  $\mathbf{E}$  represents any applied electric field that is tangent to the surface.<sup>27</sup> In MST, the poloidal drive is applied through a sequence of pulses.<sup>12</sup> In our simulations, we average this into a square pulse that removes 20%–25% of the toroidal magnetic flux over the pulse, as in the experiment. The duration of the pulse, hence the magnitude of the applied  $E_\theta$ , is scaled according to nonlinear dynamics such as the sawtooth period,<sup>24,25</sup> roughly  $S^{-0.4}$  or  $S^{-0.5}$ . Thus, a pulse duration of approximately  $0.007\tau_r$  in the MST experiment at  $S \cong 10^6$  is scaled to  $0.045\tau_r$  in our simulations at  $S=8000$ . When including programming of the axial electric field,  $E_z$  at the wall is decreased to 0 over the same time that the poloidal current drive is applied. However, as discussed below, a number of our simulations consider the poloidal drive in isolation to distinguish different effects.

Since there is no geometric variation in the axial coordinate, quadratic quantities may be uniquely decomposed by Fourier index. This includes magnetic energy and kinetic energy with the assumption of fixed uniform mass density. For all indices except the symmetric  $n=0$ , there is no flux of energy through the plasma surface, and apart from the error noted earlier, the modal energy evolves as

$$\begin{aligned} & \frac{\partial}{\partial t} \int (|B_n|^2/\mu_0 + \rho|V_n|^2) d\text{Vol} \\ &= \int [\mathbf{V}_n^* \cdot (\mathbf{J} \times \mathbf{B})_n - \mathbf{J}_n^* \cdot \mathbf{E}_n - \rho\nu(\nabla\mathbf{V}_n^*)^T : \nabla\mathbf{V}_n] d\text{Vol} \\ &+ \text{c.c.}, \end{aligned} \quad (3)$$

where the asterisk denotes the complex conjugate operation, and “c.c.” indicates the complex conjugate of the preceding term.<sup>30</sup> As in Ref. 20, it is useful to decompose the first two terms on the right side of Eq. (3) into interactions with the  $n=0$  component, i.e., the “mean,” hereafter indicated by  $\langle \rangle$ , and interaction with other nonsymmetric components,

$$(\Omega_{\text{MF}})_n = \int [-\langle \mathbf{J} \rangle \cdot \mathbf{V}_n^* \times \mathbf{B}_n - \langle \mathbf{V} \rangle \cdot \mathbf{J}_n^* \times \mathbf{B}_n] d\text{Vol} + \text{c.c.}, \quad (4)$$

$$(\Omega_{\text{MC}})_n = \int [\mathbf{V}_n^* \cdot (\mathbf{J} \times \mathbf{B})_n + \mathbf{J}_n^* \cdot (\mathbf{V} \times \mathbf{B})_n] d\text{Vol} + \text{c.c.}, \quad (5)$$

$$(\Omega_D)_n = - \int [\eta\mathbf{J}_n^* \cdot \mathbf{J}_n + \rho\nu(\nabla\mathbf{V}_n^*)^T : \nabla\mathbf{V}_n] d\text{Vol} + \text{c.c.}, \quad (6)$$

where subscripts indicate mean-field interaction (MF), coupling among modes (MC), and dissipation (D). Note that although terms that are linear in  $\langle \mathbf{V} \rangle$ ,  $\langle \mathbf{B} \rangle$ , and  $\langle \mathbf{J} \rangle$  are included in Eq. (3), they are implicitly excluded from the quadratic factors in parentheses in Eq. (5). The three powers are

recorded in our nonlinear simulations, and some of the figures presented later sum contributions over representative groups of fluctuations.

A complementary diagnostic performs linear stability analysis on mean-field profiles taken from the nonlinear simulations at various times during a transient. Technically,  $\langle \mathbf{J} \rangle \times \langle \mathbf{B} \rangle \neq \mathbf{0}$  in these profiles, but for 3% fluctuation levels, the dominant discrepancy from correlated fluctuations is necessarily small. We also emphasize that the linear computations are not predictions of nonlinear evolution. In addition to power from nonlinear coupling ( $\Omega_{\text{MC}}$ ), nonlinear effects distort the fluctuations from the linear eigenmode profiles,<sup>29</sup> so the mean-field transfer ( $\Omega_{\text{MF}}$ ) is not the same as a quasi-linear computation. Nonetheless, linear analysis of the evolving mean profiles indicates the change in free energy available to drive fluctuations. Moreover, since the linearly independent solutions used to construct eigenmodes are found from initial-value computations in radius, deviations in the ordinary differential equation solutions indicate the radial location where the PPCD pulse penetration effects a change in stability. We have found this to be much more informative than comparing profiles of the energy density transfer to the mean field; i.e., the integrand in Eq. (4).

Our linear analyses solve the zero-beta, helical flux form of Newcomb's equation for outer ideal regions,<sup>4</sup>

$$\begin{aligned} \frac{d^2\psi}{dr^2} = \psi \left[ \frac{m^2 + k^2r^2}{r^2} - \frac{m^4 + 10m^2k^2r^2 - 3k^4r^4}{4r^2(m^2 + k^2r^2)^2} - \lambda^2 \right. \\ \left. + \frac{d\lambda}{dr} \left( \frac{m\langle B_z \rangle + kr\langle B_\theta \rangle}{m\langle B_\theta \rangle - kr\langle B_z \rangle} \right) + \frac{2\lambda mk}{m^2 + k^2r^2} \right], \end{aligned} \quad (7)$$

with the  $e^{i(m\theta - kz)}$  convention, where  $\psi = r^{3/2}B_{r'}(m^2 + k^2r^2)^{1/2}$ ,  $k = 2\pi n/L_z$  is the axial wavenumber, and  $\lambda \equiv \mu_0 \langle \mathbf{J} \rangle \cdot \langle \mathbf{B} \rangle / \langle \mathbf{B} \rangle \cdot \langle \mathbf{B} \rangle$  is the normalized parallel current density. The mean profile from a nonlinear NIMROD simulation can be transferred to an eigenvalue code that solves Eq. (7) for initial-value (in  $r$ ) problems within regions that are bounded by the axis and the rational surface or by the rational surface and the wall. (All of the linear computations considered here have only one rational surface at most.) Only one nontrivial solution adjacent to the axis satisfies regularity at  $r=0$ . This solution is smoothly extended into the next outer region using Robinson's comparison equation.<sup>4</sup> A second linearly independent solution with  $\psi(r_s)=0$  and  $d\psi/dr|_{r_s}=1$  is computed for  $r_s \leq r \leq a$ , where  $r_s$  is the radius of the rational surface and  $a$  is the wall radius. The two solutions are combined to satisfy boundary conditions at the wall, and this provides the eigenvalue. With  $\psi_c$  denoting the solution that is continuous and smooth at  $r_s$  and  $\psi_i$  denoting the second solution extended to satisfy  $\psi_i(r)=0$ ,  $0 \leq r \leq r_s$ , the tearing-mode eigenvalue and stability parameter that makes the combined solution equal to zero at the wall is

$$\Delta' = \frac{d\psi/dr|_{r_s^+} - d\psi/dr|_{r_s^-}}{\psi(r_s)} = - \frac{\psi_c(a)}{\psi_i(a)\psi_c(r_s)}. \quad (8)$$

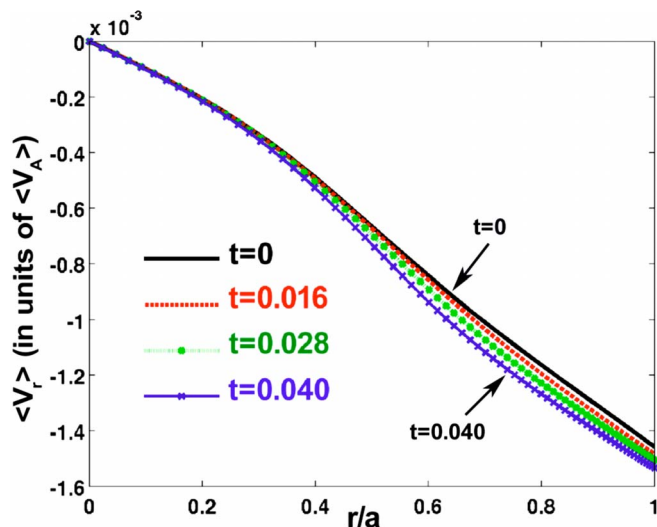


FIG. 1. (Color online) Evolution of  $\langle V_r \rangle$  profile from the symmetric computation with poloidal electric field applied at  $t=0$ .

Since this is only meaningful in ideally stable conditions, where  $\psi_c(r_s) > 0$  and  $\psi_t(a) > 0$ , the sign of  $\psi_c(a)$  determines the tearing-mode stability for the wavenumber pair  $(m, n)$  under consideration. Thus, radially localized changes in the profile that bend  $\psi_c(r)$  toward the  $\psi=0$  axis can be interpreted as destabilizing, while changes that bend  $\psi_c(r)$  away from the axis are stabilizing, as discussed in Ref. 16.

### III. PROFILE EVOLUTION WITHOUT FLUCTUATIONS

When PPCD is successful at removing fluctuations, the system becomes an evolving one-dimensional (1D) profile. For comparison, it is therefore useful to consider 1D profile evolution in the conditions of our complete simulations before considering the role of fluctuations. The computations are similar to the profile evolution considered in Ref. 19, except that we use lower S-value, and an effective small flux of mass prevents a vacuum region from opening. The computations are started from an Ohmic equilibrium with pinch and reversal parameters of  $\Theta=1.56$  and  $F=0.01$ , respectively, where  $\Theta \equiv \mu_0 a I_z / 2\Phi_z$ ,  $F \equiv \pi a^2 \langle B_z(a) \rangle / \Phi_z$ ,  $I_z$  is the axial current, and  $\Phi_z$  is the axial flux. They are initially driven by axial electric field alone.

When a pulse of poloidal electric field is applied without changing axial electric field, the initial effect in the profile is an increase in parallel current density near the edge. It propagates inward initially due to the large resistivity. However, the toroidal flux is removed faster than global diffusion, leading to increasingly negative toroidal field at the wall. The magnetic field near the wall therefore becomes perpendicular to the applied electric field, and the pinch flow associated with  $\mathbf{E} \times \mathbf{B}$  drift increases, as shown in Fig. 1. As this continues, what started as a flattening of the  $\lambda$ -profile through additional edge current becomes a pinching of the  $\lambda$ -profile that concentrates the profile in the core region, as shown in Fig. 2(a). In contrast, when the axial electric field is simultaneously reduced, the expansion of the magnetic field at the

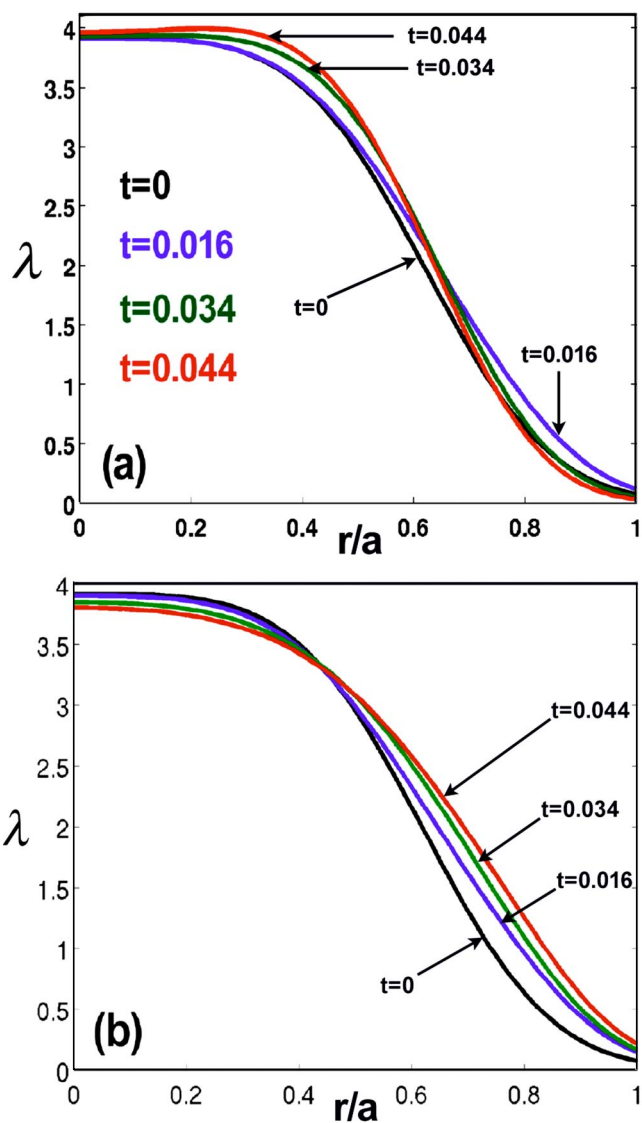


FIG. 2. (Color online) Evolution of “parallel current density,”  $\lambda \equiv \mu_0 a \langle \mathbf{J} \cdot \langle \mathbf{B} \rangle / \langle B \rangle^2$  from symmetric computations with poloidal electric field applied at  $t=0$  and (a) fixed toroidal electric-field drive and (b) linearly decreasing toroidal drive.

wall is relatively constant. Here, the poloidal pulse is able to drive current without enhanced pinching, as shown in Fig. 2(b).

### IV. PPCD WITH A SINGLE MAGNETIC ISLAND

To examine the stabilizing effects of PPCD without the complication of modal coupling, we first consider a simplified case where only one tearing perturbation is present. A configuration with a single saturated island is created from a tearing unstable Ohmic equilibrium at aspect ratio  $L_z/2\pi a = 1$  with a safety factor profile ( $q=2\pi r \langle B_z \rangle / L_z \langle B_\theta \rangle$ ) that is approximately  $2/3$  on axis and slightly greater than 0 at the wall. The  $(1,2)$  mode is linearly unstable, and other modes are precluded in this set of simulations by evolving the limited set of axial harmonics  $0 \leq n \leq 2$ . Nonlinearly, it saturates at amplitude of approximately 10% of the mean-field amplitude, which creates a magnetic island that covers more than

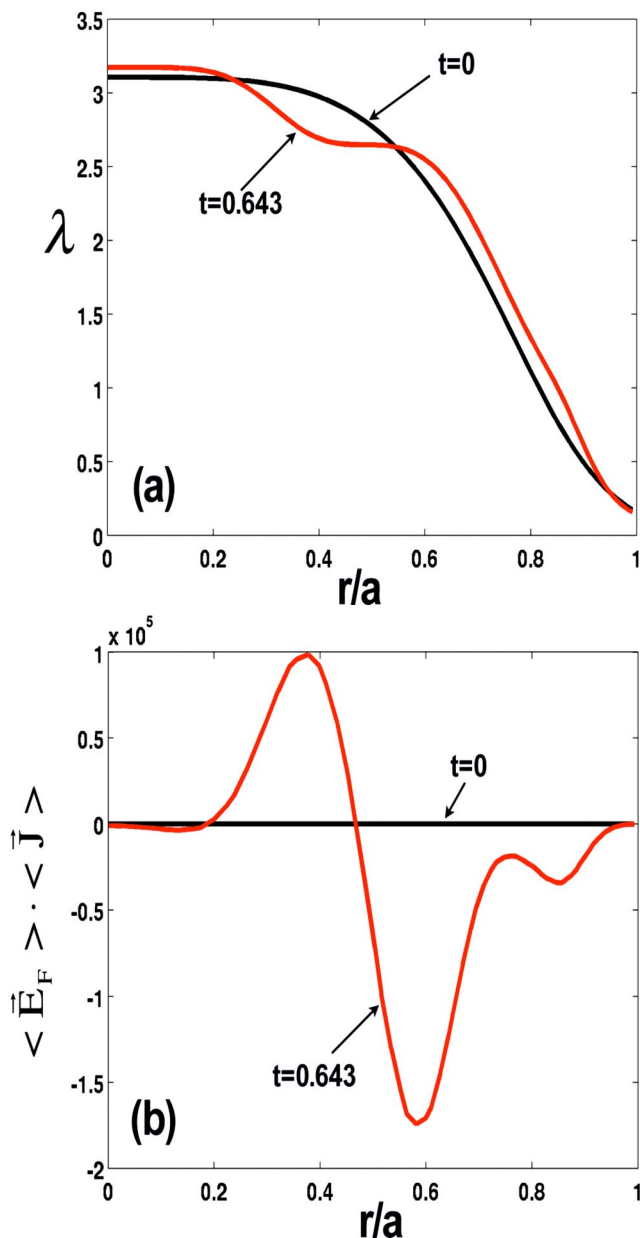


FIG. 3. (Color online) Profiles of (a) parallel current density and (b) dynamo drive  $\langle \mathbf{J} \cdot \langle \mathbf{E}_F \rangle$ , where  $\langle \mathbf{E}_F \rangle = -\mathbf{V}_n^* \times \mathbf{B}_n + \text{c.c.}$ , for  $n=2$  before and after saturation for the single-mode computation.

50% of the radial dimension. The  $\lambda$ -profile is flattened in the vicinity of the rational surface ( $r_s=0.48a$ ), as shown in Fig. 3(a) through the dynamo effect shown in Fig. 3(b). While the saturated (1,2) fluctuation has a slightly different profile than the linear eigenfunctions, linear analysis of the mean profile finds that the (1,2) mode is essentially stable with  $\Delta'$  being orders of magnitude smaller than its value of 38 in the initial symmetric equilibrium. With respect to the nonlinear power diagnostics for the  $n=2$  fluctuation, the rate of energy transfer from the mean field,  $\Omega_{MF}=0.059$  (in units of  $\pi a^2 L_z B_0^2 / 2\mu_0 \tau_r$ ) balances the dissipation  $\Omega_D = -0.059$ , as expected when no other interaction exists.

Poloidal electric field scaled to remove 20% of the toroidal flux over  $0.045\tau_r$  is applied to modify the saturated state with an inductive transient. As shown in Fig. 4, a sig-

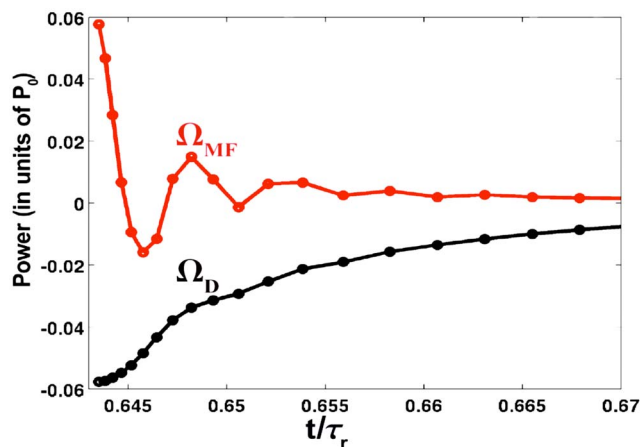


FIG. 4. (Color online) Evolution of  $\Omega_{MF}$  and  $\Omega_D$  for  $n=2$  from the single-mode computation. The powers are reported in  $P_0 \equiv \pi a^2 L_z B_0^2 / 2\mu_0 \tau_r$ .

nificant reduction in  $\Omega_{MF}$  occurs promptly within  $0.002\tau_r$  of applying the pulse at  $0.643\tau_r$ . The dissipation indicated by  $\Omega_D$  changes more slowly, and the amplitude of the fluctuation decreases over the duration of the pulse. The change in parallel current after  $0.002\tau_r$  is isolated to the edge of the plasma, as shown in Fig. 5. However, after another  $0.001\tau_r$ , a global change in the  $\lambda$ -profile becomes apparent. This global change is a result of the loss of dynamo effect as the amplitude of the fluctuation decreases.

With  $\Omega_{MF}$  changing so quickly with PPCD and the global nature of the (1,2) perturbation, appreciable change in free energy is unexpected as the initial stabilization mechanism. However, linear analysis of the sequence of profiles produced in the nonlinear simulation indicates that this is the case. As shown in Fig. 6, the smooth  $\psi_c$  solution of Eq. (7) for conditions  $0.001\tau_r$  into the pulse is affected by PPCD-driven current near the wall. The value of  $\psi_c(a)$  initially increases above 0, which indicates a stabilizing influence according to the discussion in Sec. II. The subsequent stabilization is similar to the effect of edge current noted in Ref. 19. However, slightly later in our nonlinear simulation, non-

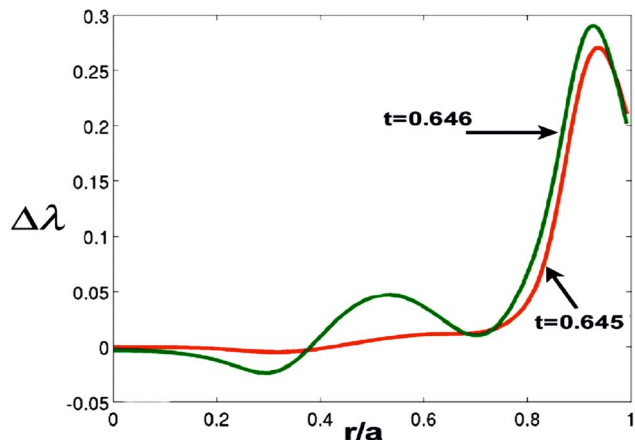


FIG. 5. (Color online) Profiles of  $\Delta\lambda = \lambda(r, t) - \lambda(r, t_p)$ , where  $t_p = 0.643\tau_r$  is the time of pulse application, from the single-mode computation. The  $m=1$ ,  $n=2$  resonance is still at  $r_s=0.48a$  at the times shown in the figure.

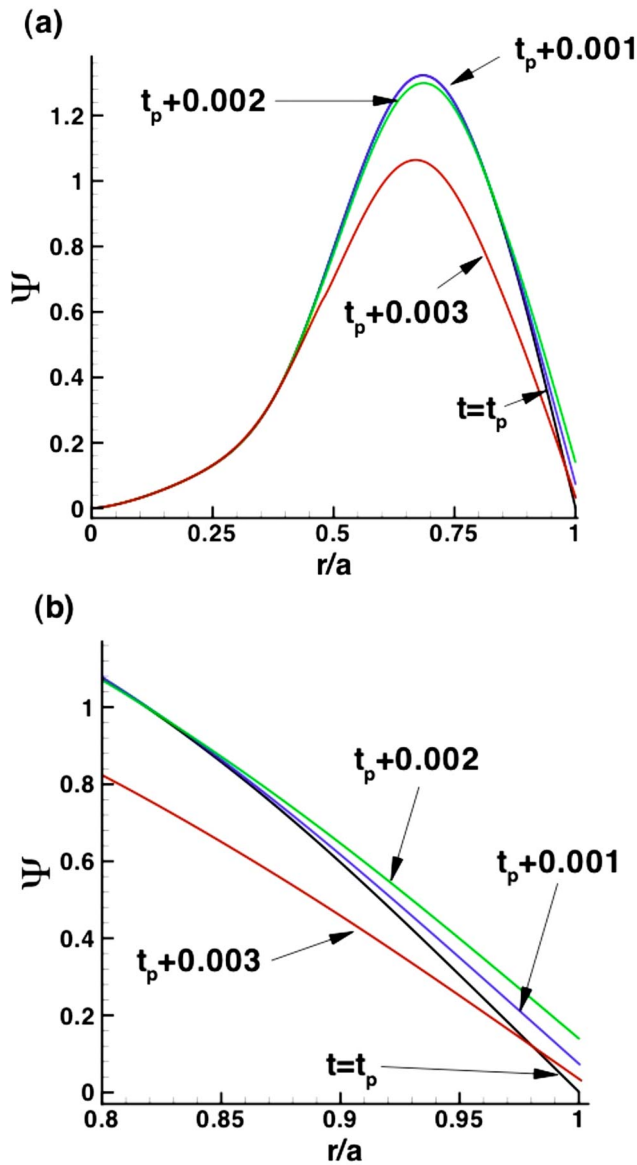


FIG. 6. (Color online) Traces of the smooth solution to Eq. (7) computed for the  $m=1$ ,  $n=2$  mode using profiles from the island-suppression computation at times shortly after pulse application ( $t=t_p$ ). Details in the edge region are shown in (b).

local profile changes due to loss of dynamo begin to occur, and the gradient in the  $\lambda$ -profile near the rational surface builds. This leads to the destabilizing influence of  $\psi_c$  bending downward at  $r=0.4a$  that is evident in the solution for conditions  $0.003\tau_r$  into the pulse, shown in Fig. 6(a).

In the nonlinear simulation, the (1,2) fluctuation does not return. The evolution late in the pulse shows that the  $q$ -profile continually decreases across the radius, so the rational surface of the (1,2) mode moves toward the axis [Fig. 7(a)]. The pinching produces a somewhat hollow parallel current density profile [Fig. 7(b)], and the gradient at the rational surface of the (1,2) becomes positive which is a stabilizing influence. However, the increasingly concentrated parallel current density would drive other fluctuations if a greater range of axial harmonics were included in the simulation. This is considered in the following section.

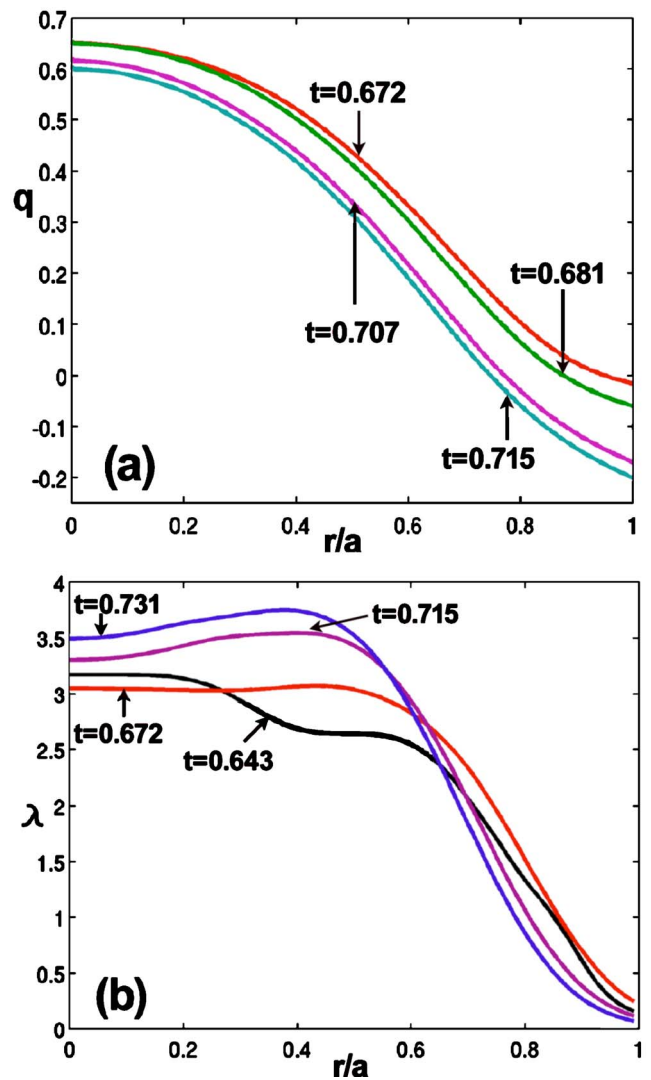


FIG. 7. (Color online) Evolution of (a) safety factor  $q=2\pi r\langle B_z\rangle/L_z\langle B_\theta\rangle$  and (b) parallel current density profiles throughout the pulse application in the island-suppression computation.

## V. PULSED DRIVE IN MULTIHELICITY CONDITIONS

The single-island evolution considered in the previous section is a significant simplification of the dynamic conditions present in multihelicity simulations and in experiments. There are many low-order resonant modes in the RFP, and their interaction helps transfer energy from unstable modes at any point in time. The nonlinear coupling also distorts the shape of the perturbed fields, so interaction with the mean profile is not entirely described from a quasilinear approach. In addition, above very low values of  $S$  where all but a dominant helicity is damped,<sup>31</sup> the saturated states are dynamic.<sup>20,24</sup> In the range of  $S$ -values considered here, the fluctuations exhibit random behavior where the ordering with respect to energy content exchanges among a group of interior-resonant fluctuations (predominantly  $m=1$ ), as shown in Fig. 8 for a  $L_z/2\pi a=3$  simulation with  $0\leq n\leq 42$  without PPCD. The mean profiles are not steady in the saturated state, but  $q(0)$  does not exceed 0.2 with the axial drive holding  $\Theta\cong 1.61$  and shallow reversal of  $F\cong -0.04$ .

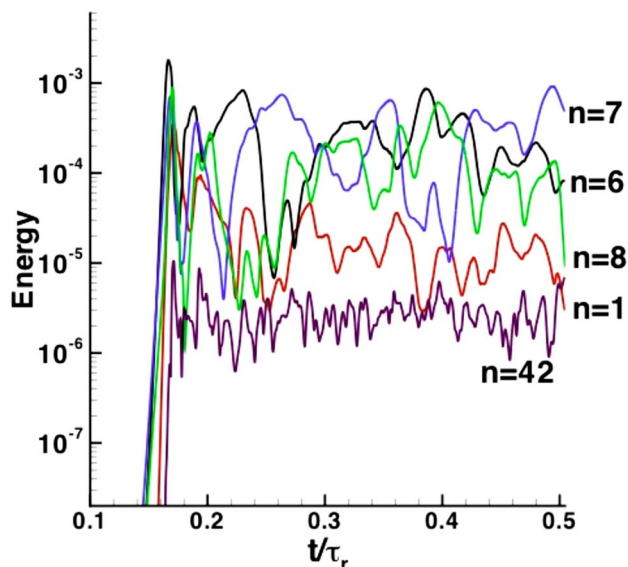


FIG. 8. (Color online) Evolution of normalized magnetic fluctuation energy,  $(2/\pi a^2 L_z B_0^2) \int |B_n|^2 dVol$ , for a subset of the Fourier components of the simulation of standard RFP dynamics.

Here, the group of fluctuations most likely to remove energy from the interior of the profile, the “core” resonant modes, includes  $m=1$ ,  $6 \leq n \leq 12$ . A comparison of the  $\Omega_{MF}$  and  $\Omega_{MC}$  for individual fluctuations in this group over an interval of  $0.08\tau_r$  (Fig. 9) shows important properties of the saturated state. The tendency to transfer energy into each of these fluctuations is indicated by  $\Omega_{MF} > 0$ , and  $\Omega_{MC} < 0$  shows direct loss through nonlinear coupling to other fluctuations. When summed over the group, as in Fig. 10(a), we see that the coupling loss is comparable to direct dissipation  $\Omega_D$ . The sum of  $\Omega_{MF}$ ,  $\Omega_{MC}$ , and  $\Omega_D$  is small relative to  $\Omega_{MF}$ , but its nonzero value indicates that the saturated state is not perfectly steady in time. The (1, 5) fluctuation is occasionally resonant in this simulation, but it does not grow to large amplitude. Thus, the entire  $1 \leq n \leq 5$  range is dominated by the resonant  $m=0$  fluctuations, which tend to be driven nonlinearly through coupling among different  $m=1$  fluctuations.<sup>20</sup> The  $13 \leq n \leq 42$  fluctuations tend to dissipate energy. As shown in Fig. 10(b), this group receives and dissipates as much energy from nonlinear interaction with the other groups as it does from interaction with the mean field.

With unsteady behavior in the mean profiles and in the perturbations, it is important to consider several different states upon which to apply PPCD. States including relatively shallow and deep reversal, hence relatively low and high fluctuation amplitude, are labeled numerically in Fig. 11. We first apply poloidal current drive alone, as in Sec. IV, and later in combination with decreasing toroidal drive for each of the states from the standard-RFP simulation. (To distinguish the PPCD simulations by initial state, we refer to them as “Trials” with the numerical labels provided in Fig. 11.) In addition, because standard RFP conditions are not stationary, we consider the influence of the pulses relative to the evolution in the RFP simulation without PPCD. The poloidal electric field removes 25% of the toroidal flux in the scaled interval of  $0.045\tau_r$  in each computation.

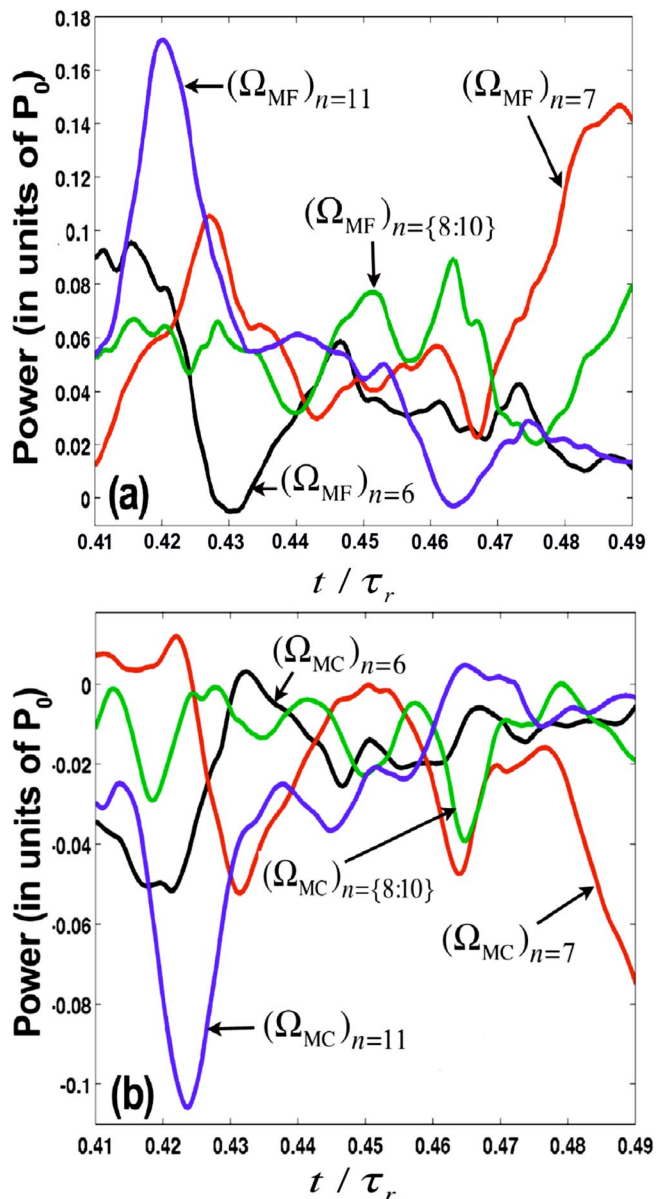


FIG. 9. (Color online) Evolution of (a)  $\Omega_{MF}$  and (b)  $\Omega_{MC}$  for the indicated core-resonant modes from the simulation of RFP dynamics without PPCD.

In all of the numerical trials, the poloidal pulse leads to a substantial decrease in the magnetic fluctuation level, as shown in Fig. 12. The weakest response results in Trial 4, which begins  $0.471\tau_r$  into the standard-RFP simulation. Here, the fluctuations start from relatively low amplitude. Trials 1 and 2 start from relatively high fluctuation levels, and the effect of PPCD is greatest. Trials 3 and 5 are started when at least one of the core fluctuations in the standard-RFP simulation is growing significantly. The fluctuation amplitude continues to increase briefly before the poloidal pulse reverses the trend. Late in each of the poloidal pulse trials, the fluctuation levels grow rapidly.

The total power flowing from the mean profile into fluctuations, i.e.,  $\Omega_{MF}$ , begins to decrease within the first  $0.001\tau_r$  ( $16\tau_A$ ) into the pulse for each of the five states. This rapid response in  $\Omega_{MF}$  is primarily in the group of core fluctuations and in the high- $n$  fluctuations, as shown in Figs. 13 and 14.

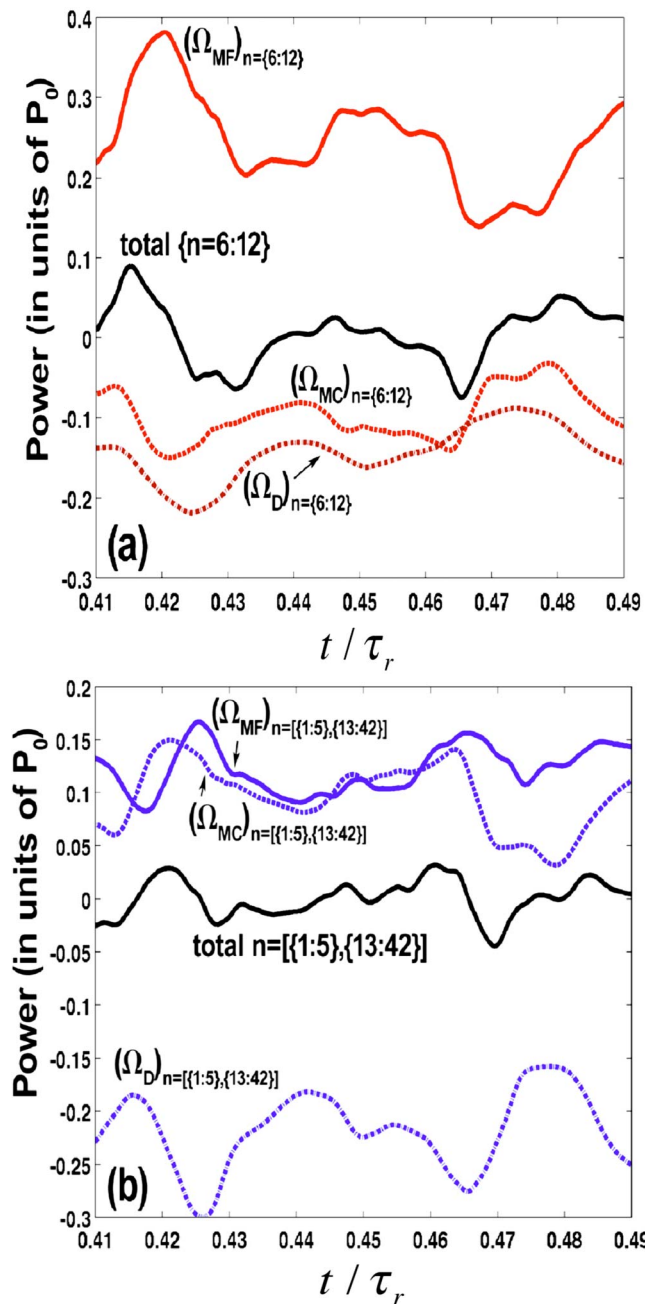


FIG. 10. (Color online) Evolution of  $\Omega_{MF}$ ,  $\Omega_{MC}$ , and  $\Omega_D$  summed over (a) interior-resonant fluctuations and (b) other fluctuations from the simulation of RFP dynamics without PPCD.

For both groups, the  $\Omega_{MF}$  powers quickly drop below the levels in the standard-RFP evolution. Also note that the nonlinear coupling power ( $\Omega_{MC}$ ) responds more slowly for both groups. This contributes to the rapid decrease in fluctuation energy for the core modes. In contrast, interaction with the mean profile  $\Omega_{MF}$  is relatively slow to respond for the  $m=0$  group (Fig. 15), but the equally significant coupling power  $\Omega_{MC}$  responds almost as quickly as  $\Omega_{MF}$  for the core group. Like the single-island case described in Sec. IV, it is clear that the pulse affects the fluctuations through profile changes, but we see that it is an indirect process for the  $m=0$  fluctuations.

Although the multihelicity states are more dynamic than

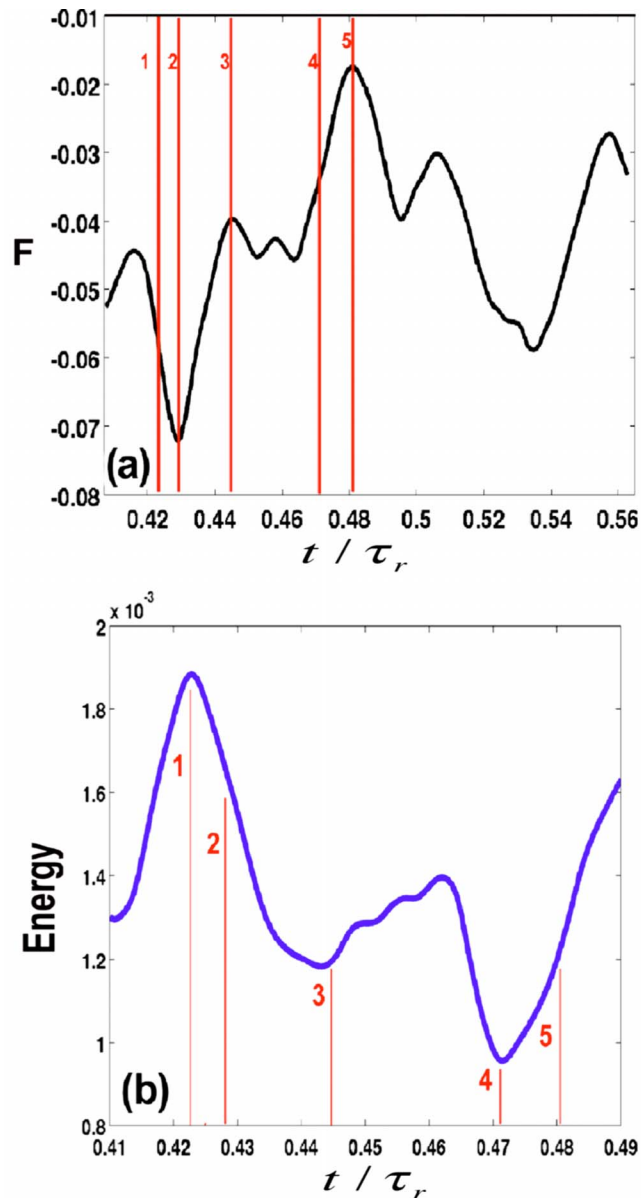


FIG. 11. (Color online) Evolution of (a) reversal parameter  $F$  and (b) total magnetic fluctuation energy relative to  $E_0 \equiv \pi a^2 L_z B_0^2 / 2\mu_0$  from the simulation of RFP dynamics without PPCD. Numerical labels for five representative states are shown in the plots.

the case considered in Sec. IV, linear analysis applied to sequences of profiles from nonlinear simulations again helps locate the stabilizing influence. In Trial 5, for example, we observe that the smooth solution of Eq. (7) is distorted upward near the wall, as shown in Fig. 16 for the (1,7) and (1,13) helicities. The pulse-induced distortion is small for the (1,7) helicity relative to the effects of natural profile evolution. This is typical, but since the conditions are in a saturated state, a small stabilizing influence for the dominant fluctuations is enough to change the evolution completely. Also evident in Fig. 16, the effect of the pulse on  $\psi_c$  extends over most of the radius only a few thousands of  $\tau_r$  later. Pinching from loss of dynamo quickly begins to obscure the initial stabilization mechanism; however, fluctuation suppression continues. We note that the linear computations do

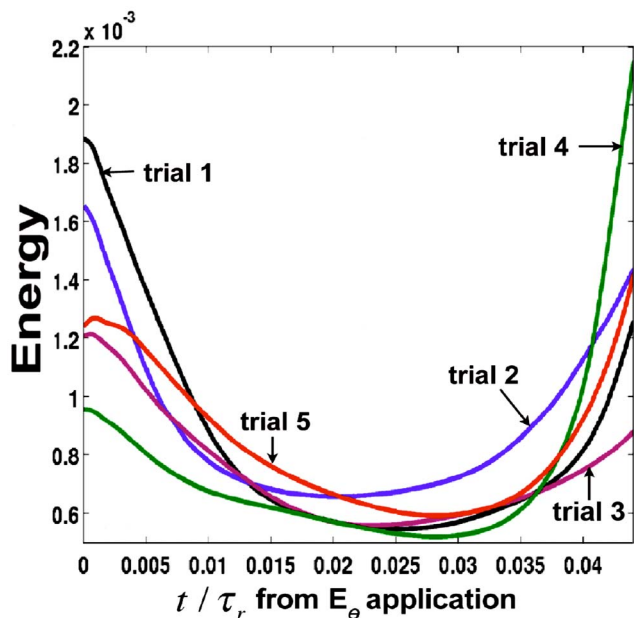


FIG. 12. (Color online) Evolution of total fluctuation energy relative to  $E_0 \equiv \pi a^2 L_z B_0^2 / 2\mu_0$  from each of the PPCD pulse application trials for multihelicity conditions.

not always provide an indication of the suppression, even for the core modes that are driven by power transfer from the mean field. We observe that the shape of the largest fluctuation tends to follow the linear eigenmode. However, other fluctuations tend to be distorted by nonlinear coupling, and when this distortion is significant as in Trial 1, where the pulse is applied at a relative peak in fluctuation activity, the predicted trend from the linear computation may be incorrect until the coupling power is reduced.

The reduction of fluctuations continues over at least  $0.01\tau_r$  in our poloidal-drive simulations, an order of magnitude longer than the timescale of the initial response. As in the single-island computation, significant profile changes result from the loss of dynamo effect, and the gradually increasing concentration of parallel current density in the core begins to destabilize the core-resonant modes. Similar to computations without fluctuations (Sec. III), removing toroidal flux without a reduction of toroidal drive leads to increased pinching in the core, as shown in the  $\lambda$ -profile evolution for Trial 2 in Fig. 17. With many helicities included in a simulation, one or more will eventually become unstable, leading to the large growth of fluctuation energy evident near the end of the pulse in Fig. 12.

The one-dimensional computations described in Sec. III demonstrate that reducing the toroidal drive counteracts the pinching from the poloidal drive. When used together for each of the five trial states from the standard-RFP simulation, the growth in fluctuation energy near the end of the pulse is completely avoided, shown in Fig. 18(a). Unlike the computations with poloidal drive alone, there is no increase in  $\Omega_{MF}$  near the end of each pulse [Fig. 18(b)]. However, the interaction with the mean field is essentially independent of the toroidal drive over the first  $0.01\tau_r$  of the pulse for each state. Linear computations again show that the enhanced parallel

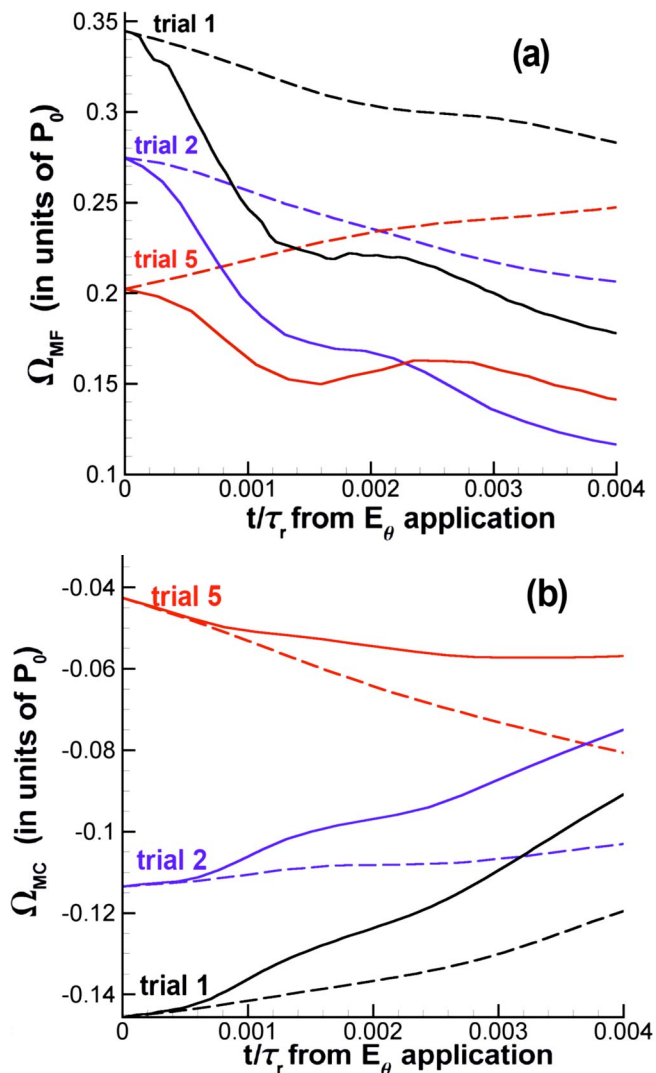


FIG. 13. (Color online) Evolution of (a)  $\Omega_{MF}$  and (b)  $\Omega_{MC}$  for the interior-resonant group  $6 \leq n \leq 12$  from the multihelicity PPCD trials indicated. The solid traces show results with poloidal electric-field pulsing, and dashed traces show results without pulsing for comparison. The first 10% of the pulse duration is plotted to highlight prompt responses.

current density from the poloidal drive in the edge of the plasma is responsible for the initial stabilization. The role of reducing the toroidal drive is then to maintain the low fluctuation level as long as possible. In fact, the system is able to continue to the dynamo-free state reported in Refs. 7 and 8 for MST. The stochasticity of the magnetic field topology is dramatically reduced near the end of the pulse, as shown in Fig. 19 for Trial 4.

## VI. CONCLUSIONS

The full dynamics of tearing mode stabilization by electric field programming involves a combination of effects. The programming modifies both the energy transfer between the tearing modes and the mean field, and between different tearing modes. Our computations show that the effects are somewhat separated in time. Initially and rapidly, the flow of energy from the mean field to the dominant core-resonant

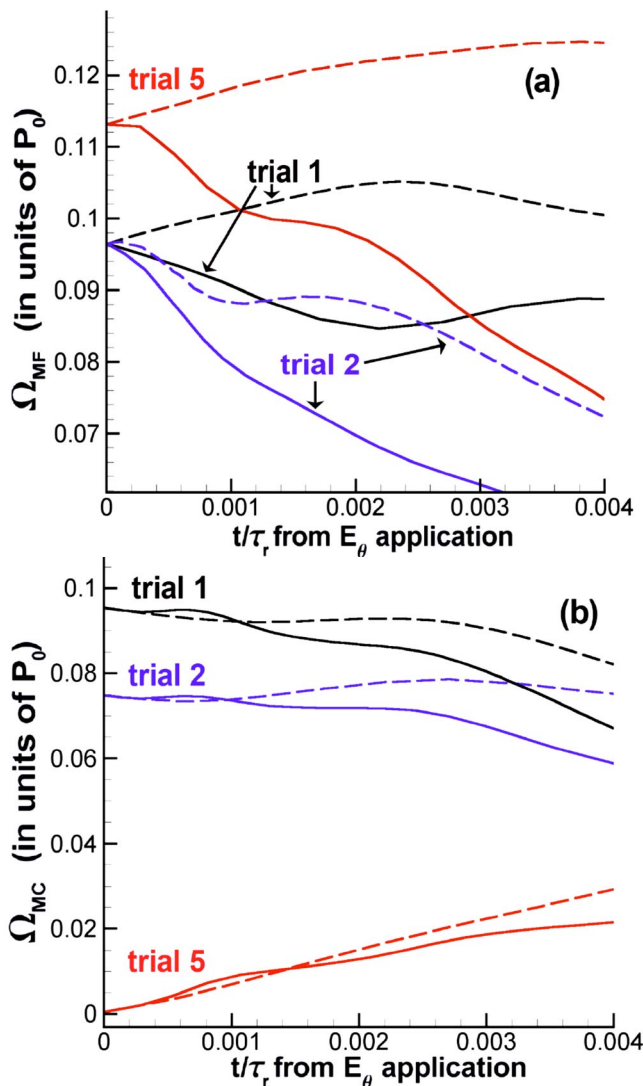


FIG. 14. (Color online) Evolution of (a)  $\Omega_{MF}$  and (b)  $\Omega_{MC}$  for the high- $n$  group from the multihelicity PPCD trials indicated.

tearing modes is altered. This results from a slight change in the parallel current profile near the wall, consistent with trends in linear stability analysis and with motivations<sup>9</sup> for PPCD. While the drive for instability is reduced for the dominant core fluctuations very shortly after the pulse is applied, nonlinear coupling (an energy sink for this group) responds relatively slowly. Thus, powers affecting these fluctuations become unbalanced, so they lose energy.

The induced profile changes that lead to the initial stabilization are small relative to natural oscillations in the standard-RFP simulation. However, they are large enough to alter the balance between energy transfer from the profiles, coupling among fluctuations, and dissipation in a nonlinearly saturated state. Our simulation that applies PPCD to a single saturated tearing mode is an illustrative, albeit unrealistic, example. The saturated mean profile is marginally stable, and any flattening of the current profile reduces the fluctuation amplitude. In full RFP simulations, the saturated state without PPCD is not perfectly steady, but it, too, is sensitive to changes in the drive of the dominant fluctuations. There is

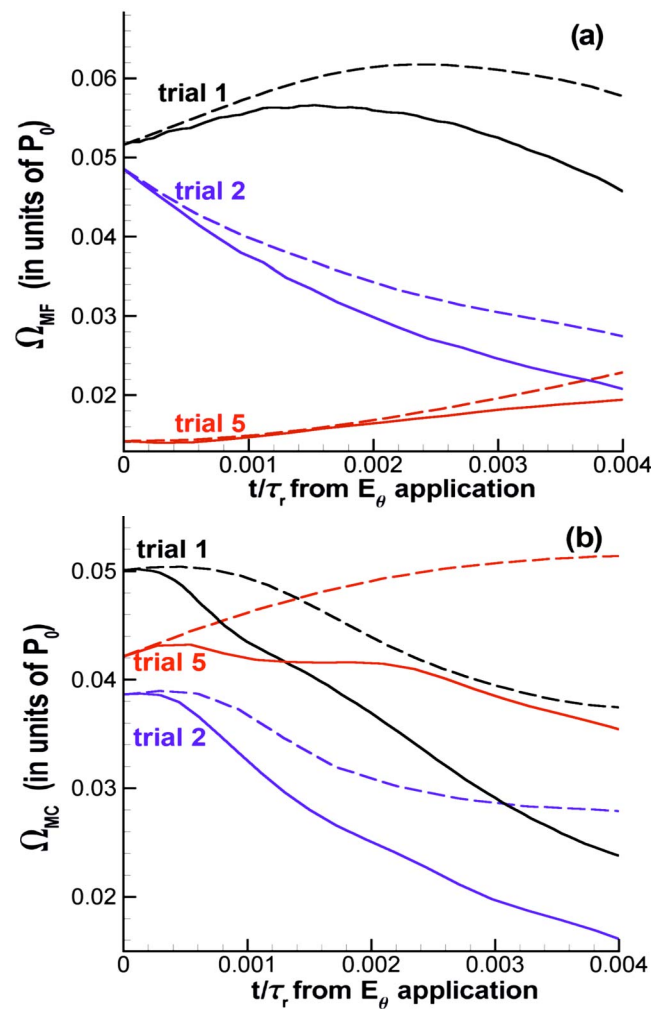


FIG. 15. (Color online) Evolution of (a)  $\Omega_{MF}$  and (b)  $\Omega_{MC}$  for the low- $n$  ( $m=0$ ) group from the multihelicity PPCD trials indicated.

also feedback on the mean profile evolution. When fluctuation amplitudes decrease, the dynamo effect diminishes, leading to nonlocal profile changes that tend to obscure the stabilizing effect.

The response for the nonlinearly driven low- $n$  ( $m=0$ ) fluctuations is distinct from the core-resonant response. The important change in input power for this group is in nonlinear coupling, and it occurs after a slight delay while the core-resonant modes start responding to the profile alteration. The initial effect of PPCD on the  $m=0$  group is therefore indirect, as might be expected from their indirect but important role in the dynamo process.<sup>20</sup> While the high- $n$  fluctuations also receive significant power from nonlinear coupling, their response to PPCD is closer to that of the core-resonant modes. Changes in energy transfer from the mean field are first to alter their power balance, and they occur rapidly as the pulse is applied.

When comparing computations of poloidal drive with and without the reduction in toroidal drive, we have emphasized the pinching that occurs with poloidal drive alone once the dynamo effect is eliminated. Consistent with the conclusions of Ref. 12, reducing the toroidal drive keeps the inductive pulse aligned with the edge magnetic field to avoid  $\mathbf{E}$

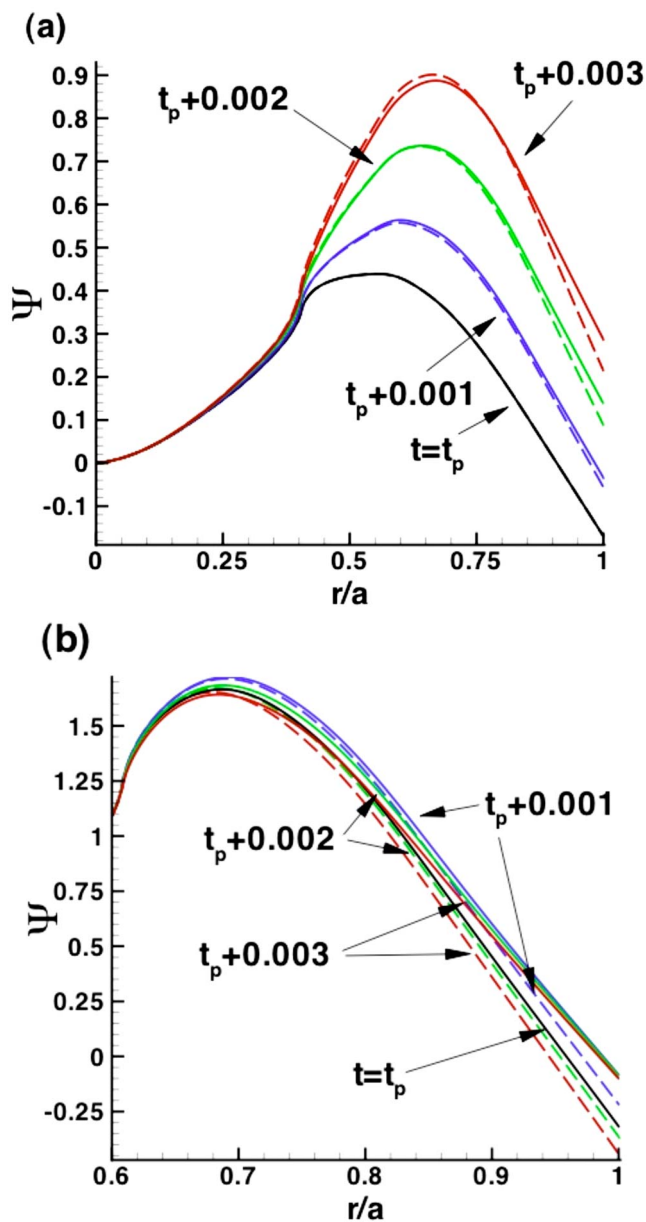


FIG. 16. (Color online) Traces of the smooth solution to Eq. (7) for (a)  $m=1, n=7$  and (b)  $m=1, n=13$  for the times from pulse application ( $t=t_p$ ) indicated in the figure for Trial 5. Solid traces are computed for profiles with pulse application, and dashed traces are for profiles without pulse application.

$\times \mathbf{B}$  drift. The transient then tends to drive edge parallel current throughout the pulse. The importance of lowering the toroidal drive is also consistent with results obtained with a localized ad hoc drive that may represent RF or other non-inductive current.<sup>16</sup> It is easier to suppress the core modes when there is less drive of parallel current density on axis while the auxiliary drive maintains parallel current density at larger radii to replace the dynamo.

Future numerical work to understand effects beyond tearing-mode stabilization, such as the emergence of  $m=0$  fluctuations,<sup>12</sup> will likely require evolution of the continuity equation, pressure-driven effects, and fluctuation-induced transport. The penetration dynamics of the applied electrical transient may also change quantitatively when temperature

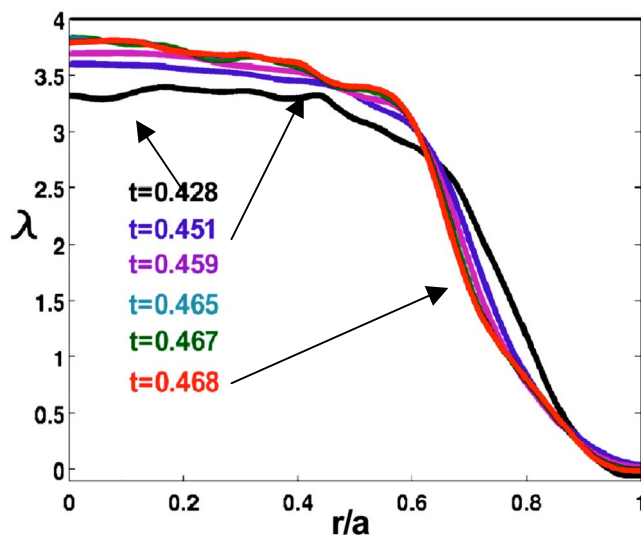


FIG. 17. (Color online) Evolution of parallel current density profile through the pulse in Trial 2 with toroidal drive maintained.

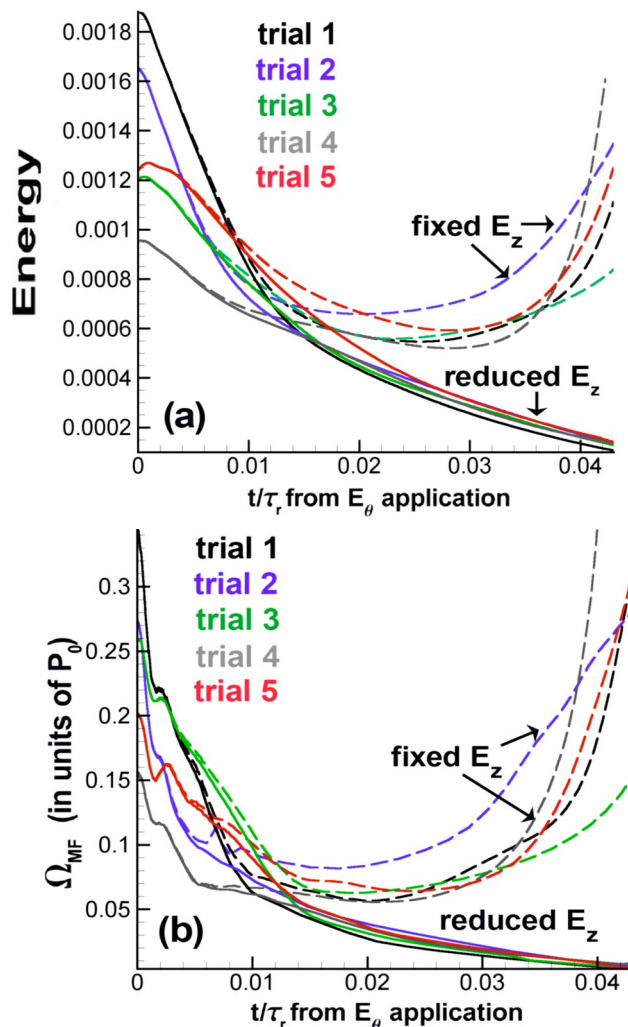


FIG. 18. (Color online) Comparison of (a) total magnetic fluctuation energy and (b)  $\Omega_{MF}$  for the interior-resonant group for multihelicity computations with poloidal pulsing with and without reduction of the toroidal drive.

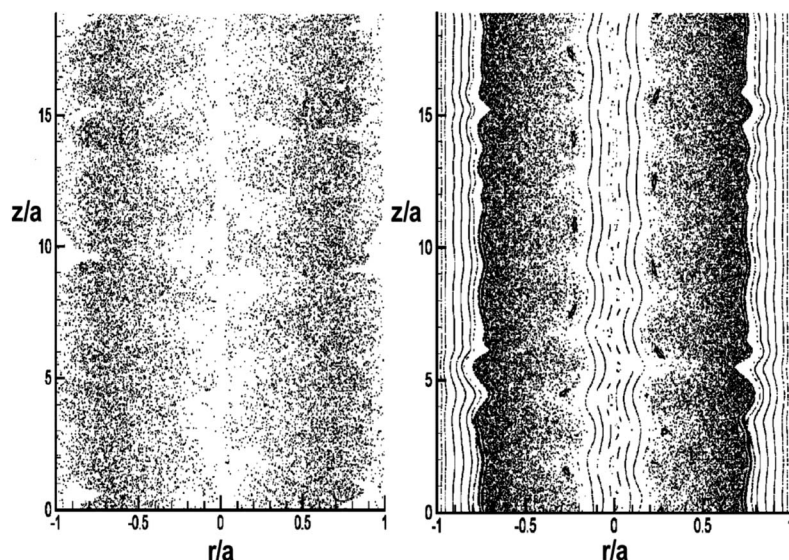


FIG. 19. Poincaré surfaces of section for magnetic field before (left) and after (right) PPCD with toroidal drive reduction for Trial 4. Plots show an entire radial-axial slice of the domain.

dependent resistivity is added to the model. Finally, resolving the full nonlinear RFP physics at more experimentally relevant Lundquist numbers is needed to investigate how PPCD pulses interact with the sawtooth cycle.

#### ACKNOWLEDGMENTS

The authors thank MST scientists J. S. Sarff, J. K. Anderson, and B. E. Chapman for insightful discussions. J.M.R. is also grateful for many excellent discussions with J. H. Cooley, G. L. Delzanno, J. M. Finn, J. Fung, T. A. Gianakon, R. A. Nebel, and E. M. Nelson. This work has been supported by U.S. Department of Energy Grant Nos. DE-FG02-02ER54687 and DE-FG02-06ER54850 and through the Los Alamos National Laboratory Applied Physics Division. The research used resources of the National Energy Research Scientific Computing Center, which is supported by the Office of Science of the U.S. Department of Energy under Contract No. DE-AC02-05CH11231.

#### APPENDIX: SCALING OF DENSITY APPROXIMATION ERRORS

We consider a simple scaling argument to support numerical findings that errors associated with using a fixed number density become small in the physically relevant limit of large  $S$ -values. First, Faraday's law combined with the ideal electric field indicates that over most of the volume (apart from tearing layers), the strength of magnetic and flow-velocity perturbations are related by  $\gamma B \sim v \langle B \rangle / L$ , where  $\gamma$  represents a nonlinear growth rate, and  $L$  is a wavelength that is related to  $a$  for global perturbations. If the growth occurs on a hybrid time for nonlinear tearing activity, i.e.,  $\gamma \sim 1/\tau_A \sqrt{S}$ , then apart from geometric factors,  $\gamma \sim v_A / L \sqrt{S}$ . We then estimate  $v \sim v_A B / \langle B \rangle \sqrt{S}$ , so for the error in the momentum density, i.e.,  $\rho \nabla \nabla \cdot \mathbf{V}$ , the scaling is  $\rho v^2 / L \sim B^2 / \mu_0 L S$ . Thus, the error is small relative to the Lorentz force density ( $\sim B^2 / \mu_0 L$ ) for large values of  $S$ . Similarly, the error in energy density, which scales as  $\rho v^3 / L \sim v B^2 / \mu_0 L S$ , is small relative to terms in the integrands of

Eqs. (4) and (5) as  $S$  becomes large. The same scaling arguments can be applied to the physical inertial terms, and the fact that they tend to be small relative to Lorentz-force terms is noted in Ref. 20.

- <sup>1</sup>S. Ortolani and D. D. Schnack, *Magnetohydrodynamics of Plasma Relaxation* (World Scientific, Singapore, 1993), Chap. 5; H. Ji, S. C. Prager, A. F. Almagri, J. S. Sarff, Y. Yagi, Y. Hirano, K. Hattori, and H. Toyama, *Phys. Plasmas* **3**, 1935 (1996).
- <sup>2</sup>G. Fiksel, S. C. Prager, W. Shen, and M. Stoneking, *Phys. Rev. Lett.* **72**, 1028 (1994); T. M. Biewer, C. B. Forest, J. K. Anderson, G. Fiksel, B. Hudson, S. C. Prager, J. S. Sarff, J. C. Wright, D. L. Brower, W. X. Ding, and S. D. Terry, *Phys. Rev. Lett.* **91**, 045004 (2003).
- <sup>3</sup>R. N. Dexter, D. W. Kerst, T. H. Lovell, S. C. Prager, and J. C. Sprott, *Fusion Technol.* **19**, 131 (1991).
- <sup>4</sup>D. C. Robinson, *Nucl. Fusion* **18**, 939 (1978).
- <sup>5</sup>V. Antoni, D. Merlin, S. Ortolani, and R. Paccagnella, *Nucl. Fusion* **26**, 1711 (1986).
- <sup>6</sup>J. S. Sarff, S. A. Hokin, H. Ji, S. C. Prager, and C. R. Sovinec, *Phys. Rev. Lett.* **72**, 3670 (1994).
- <sup>7</sup>J. K. Anderson, T. M. Biewer, C. B. Forest, R. O'Connell, S. C. Prager, and J. S. Sarff, *Phys. Plasmas* **11**, L9 (2004).
- <sup>8</sup>J. K. Anderson, J. Adney, A. Almagri, A. Blair, D. L. Brower, M. Cengher, B. E. Chapman, S. Choi, D. Craig, D. R. Demers, D. J. Den Hartog, B. Deng, W. X. Ding, F. Ebrahimi, D. Ennis, G. Fiksel, C. B. Forest, P. Franz, J. Goetz, R. W. Harvey, D. Holly, B. Hudson, M. Kaufman, T. Lovell, L. Marrelli, P. Martin, K. McCollam, V. V. Mirnov, P. Nonn, R. O'Connell, S. Oliva, P. Piovesan, S. C. Prager, I. Predebon, J. S. Sarff, G. Spizzo, V. Svidzinski, M. Thomas, and M. D. Wyman, *Phys. Plasmas* **12**, 056118 (2005).
- <sup>9</sup>J. S. Sarff, N. E. Lanier, S. C. Prager, and M. R. Stoneking, *Phys. Rev. Lett.* **78**, 62 (1997).
- <sup>10</sup>M. R. Stoneking, N. E. Lanier, S. C. Prager, J. S. Sarff, and D. Sinitzyn, *Phys. Plasmas* **4**, 1632 (1997).
- <sup>11</sup>B. E. Chapman, T. M. Biewer, P. K. Chattopadhyay, C.-S. Chiang, D. J. Craig, N. A. Crocker, D. J. Den Hartog, G. Fiksel, P. W. Fontana, S. C. Prager, and J. S. Sarff, *Phys. Plasmas* **7**, 3491 (2000).
- <sup>12</sup>B. E. Chapman, A. F. Almagri, J. K. Anderson, T. M. Biewer, P. K. Chattopadhyay, C.-S. Chiang, D. Craig, D. J. Den Hartog, G. Fiksel, C. B. Forest, A. K. Hansen, D. Holly, N. E. Lanier, R. O'Connell, S. C. Prager, J. C. Reardon, J. S. Sarff, and M. D. Wyman, *Phys. Plasmas* **9**, 2061 (2002).
- <sup>13</sup>R. A. Nebel, D. D. Schnack, and T. A. Gianakon, *Phys. Plasmas* **9**, 4968 (2002).
- <sup>14</sup>F. Ebrahimi and S. C. Prager, *Phys. Plasmas* **11**, 2014 (2004).
- <sup>15</sup>Y. L. Ho, *Nucl. Fusion* **31**, 341 (1991).
- <sup>16</sup>C. R. Sovinec and S. C. Prager, *Nucl. Fusion* **39**, 777 (1999).
- <sup>17</sup>M. E. Puiatti, S. Cappello, R. Lorenzini, S. Martini, S. Ortolani, R. Pac-

- cagnella, F. Sattin, D. Terranova, T. Bolzonella, A. Buffa, A. Canton, L. Carraro, D. F. Escande, L. Garzotti, P. Innocente, L. Marrelli, E. Martines, P. Scarin, G. Spizzo, M. Valisa, P. Zanca, V. Antoni, L. Apolloni, M. Bagatin, W. Baker, O. Barana, D. Bettella, P. Bettini, R. Cavazzana, M. Cavinato, G. Chitarin, A. Cravotta, F. D'Angelo, S. Dal Bello, A. DeLorenzi, D. Desideri, P. Fiorentin, P. Franz, L. Frassinetti, E. Gaio, L. Giudicotti, F. Gnesotto, L. Grando, S. C. Guo, A. Luchetta, G. Malesani, G. Manduchi, G. Marchiori, D. Marcuzzi, P. Martin, A. Masiello, F. Milani, M. Moresco, A. Murari, P. Nielsen, R. Pasqualotto, B. Pégourie, S. Peruzzo, R. Piovan, P. Piovesan, N. Pomaro, G. Preti, G. Regnoli, G. Rostagni, G. Serianni, P. Sonato, E. Spada, M. Spolaore, C. Taliercio, G. Telesca, V. Toigo, N. Vianello, P. Zaccaria, B. Zaniol, L. Zanotto, E. Zilli, G. Zollino, and M. Zuin, *Nucl. Fusion* **43**, 1057 (2003).
- <sup>18</sup>H. Ashida, H. Sugimoto, and H. Sakakita, *J. Phys. Soc. Jpn.* **74**, 930 (2005).
- <sup>19</sup>V. A. Svidzinski and S. C. Prager, *J. Fusion Energy* **26**, 215 (2007).
- <sup>20</sup>Y. L. Ho and G. G. Craddock, *Phys. Fluids B* **3**, 721 (1991).
- <sup>21</sup>D. D. Schnack, E. J. Caramana, and R. A. Nebel, *Phys. Fluids* **28**, 321 (1985).
- <sup>22</sup>J. A. Holmes, B. A. Carreras, T. C. Hender, H. R. Hicks, V. E. Lynch, Z. G. An, and P. H. Diamond, *Phys. Fluids* **28**, 261 (1985).
- <sup>23</sup>J. A. Holmes, B. A. Carreras, P. H. Diamond, and V. E. Lynch, *Phys. Fluids* **31**, 1166 (1988).
- <sup>24</sup>S. Cappello and D. Biskamp, *Nucl. Fusion* **36**, 571 (1996).
- <sup>25</sup>M. R. Stoneking, J. T. Chapman, D. J. Den Hartog, S. C. Prager, and J. S. Sarff, *Phys. Plasmas* **5**, 1004 (1998).
- <sup>26</sup>J. M. Reynolds and C. R. Sovinec, *Bull. Am. Phys. Soc.* **44**, 113 (2002).
- <sup>27</sup>C. R. Sovinec, A. H. Glasser, T. A. Gianakon, D. C. Barnes, R. A. Nebel, S. E. Kruger, D. D. Schnack, S. J. Plimpton, A. Tarditi, M. S. Chu, and the NIMROD Team, *J. Comput. Phys.* **195**, 355 (2004).
- <sup>28</sup>C. R. Sovinec, T. A. Gianakon, E. D. Held, S. E. Kruger, D. D. Schnack, and the NIMROD Team, *Phys. Plasmas* **10**, 1727 (2003).
- <sup>29</sup>J. M. Reynolds, Ph.D. thesis, University of Wisconsin-Madison, 2007.
- <sup>30</sup>The “double-dot” product appearing in Eq. (3) is defined in W. D. D’haeseleer, W. N. G. Hitchon, J. D. Callen, and J. L. Shohet, *Flux Coordinates and Magnetic Field Structure: A Guide to a Fundamental Tool of Plasma Theory* (Springer, Berlin, 1991), pp. 44–47, for example. The related matrix operation is to take the product of two square matrices, then evaluate the trace of the product.
- <sup>31</sup>J. M. Finn, R. Nebel, and C. Bathke, *Phys. Fluids B* **4**, 1262 (1992); S. Cappello and D. F. Escande, *Phys. Rev. Lett.* **85**, 3838 (2000).